

High Ecliptic Latitude Survey for Small Main-Belt Asteroids*

Tsuyoshi Terai¹, Jun Takahashi², and Yoichi Itoh²

¹*National Astronomical Observatory of Japan, 2-21-1 Osawa, Mitaka, Tokyo 181-8588, Japan*

²*Center for Astronomy, University of Hyogo, 407-2 Nishigaichi, Sayo-cho, Sayo-gun, Hyogo 679-5313, Japan*

tsuyoshi.terai@nao.ac.jp

ABSTRACT

Main-belt asteroids have been continuously colliding with one another since they were formed. Its size distribution is primarily determined by the size dependence of asteroid strength against catastrophic impacts. The strength scaling law as a function of body size could depend on collision velocity, but the relationship remains unknown especially under hypervelocity collisions comparable to 10 km sec^{-1} . We present a wide-field imaging survey at ecliptic latitude of around 25° for investigating the size distribution of small main-belt asteroids which have highly inclined orbits. The analysis technique allowing for efficient asteroid detections and high-accuracy photometric measurements provide sufficient sample data to estimate the size distribution of sub-km asteroids with inclinations larger than 14° . The best-fit power-law slopes of the cumulative size distribution is 1.25 ± 0.03 in the diameter range of 0.6–1.0 km and 1.84 ± 0.27 in 1.0–3.0 km. We provide a simple size distribution model that takes into consideration the oscillations of the power-law slope due to the transition from the gravity-scaled regime to the strength-scaled regime. We find that the high-inclination population has a shallow slope of the primary components of the size distribution compared to the low-inclination populations. The asteroid population exposed to hypervelocity impacts undergoes collisional processes that large bodies have a higher disruptive strength and longer life-span relative to tiny bodies than the ecliptic asteroids.

Subject headings: minor planets, asteroids — solar system: general

1. INTRODUCTION

Main-belt asteroids (MBAs) have continuously undergone self-collisional processes. The impact events are characterized by the target/impactor masses and collision velocity. When kinetic energy

*Based on data collected at Subaru Telescope, which is operated by the National Astronomical Observatory of Japan (NAOJ).

of an impactor is larger than the critical specific energy Q_D^* , the energy per unit target mass required to shatter the target and disperse half of its mass, the target is catastrophically disrupted (Davis et al. 2002). Otherwise, the target (largest fragment) retains a mass larger than half of the original, resulting cratering or gravitational reaccumulation of collisional fragments after shattering. Q_D^* is an indicator of impact strength, which depends on the body size (e.g. Housen & Holsapple 1990; Durda et al. 1998; Benz & Asphaug 1999). Q_D^* decreases with increasing diameter for asteroids less than ~ 0.1 – 1 km, called ‘strength-scaled regime’. In contrast, it increases with increasing diameter for the larger asteroids, called ‘gravity-scaled regime’. The degree of change in Q_D^* with body size is the primary determinant of a power-law size distribution of the small body population in a collisional cascade (O’Brien & Greenberg 2003).

The size distribution of MBAs down to sub-km size has been estimated by previous extensive surveys with ground-based telescopes such as Palomar-Leiden Survey (PLS; van Houten et al. 1970), Spacewatch (Jedicke & Metcalfe 1998), Sloan Digital Sky Survey (SDSS; Ivezić et al. 2001), Subaru Main Belt Asteroid Survey (SMBAS; Yoshida et al. 2003; Yoshida & Nakamura 2007), and Sub-Kilometer Asteroid Diameter Survey (SKADS; Gladman et al. 2009). In addition, infrared satellites including IRAS (Tedesco et al. 2002), AKARI (Usui et al. 2011), and WISE (Masiero et al. 2011) measured accurate diameters of numerous asteroids. Figure 1 shows the cumulative size distribution of MBAs compiled from the Asteroid Orbital Elements Database¹ (ASTORB; Bowell et al. 1994) and the survey results reported by SDSS and SMBAS. Using the observed size distributions, many studies devoted efforts for modeling the collisional evolution of MBAs via numerical simulations (Durda et al. 1998; Bottke et al. 2005a,b; O’Brien & Greenberg 2005; de Elía & Brunini 2007). It should be noted that the Q_D^* law is supposed to be a function only of asteroid size in each model.

Petit et al. (2001) presented a dynamical evolution model for primordial asteroids in the early main belt that were dynamically excited due to gravitational perturbations from Jupiter and embedded planetary embryos. In this phase, collisions between asteroids occurred at higher velocities than at present (~ 4 km sec⁻¹; Vedder 1998) because of the pumped-up eccentricities and inclinations (Bottke et al. 2005b). Bottke et al. (2005a) pointed out that Q_D^* law could be affected by varying collision velocities. They suggested a steeper Q_D^* curve in the gravity-scaled regime for 10 km sec⁻¹ collisions than that for slower collisions.

The asteroid collisional evolution among impacts with much higher velocities (i.e. $\gg 4$ km sec⁻¹; hereinafter called ‘hypervelocity’) than the mean collisions in the main belt remains unknown. Because of the technical difficulties, only a few laboratory experiments for hypervelocity collisions have been conducted (Kadono et al. 2010; Takasawa et al. 2011). The hydrocode simulations by Benz & Asphaug (1999) indicated that in the gravity-scaled regime, Q_D^* for a basalt target has similar slopes between collisions of 3 km sec⁻¹ and 5 km sec⁻¹, while Q_D^* for a icy target in 3 km sec⁻¹ collisions increases with size more steeply than that in 0.5 km sec⁻¹

¹ftp : //ftp.lowell.edu/pub/elgb/astorb.html

collisions. However, another study with impact simulations showed that the slope of Q_D^* for a basalt target in 5 km sec^{-1} collisions is shallower than that in 3 km sec^{-1} collisions (Jutzi et al. 2010). The collision-velocity dependency of the Q_D^* law has not yet been confirmed.

Investigation of an asteroid population with highly inclined orbits is an effective means to understand the material properties against hypervelocity collisions. In the main belt, asteroids with orbits inclined at higher than 15° (hereinafter called high-inclination MBAs) have the mean collision velocities exceeding $\sim 7 \text{ km sec}^{-1}$ (Farinella & Davis 1992; Gil-Hutton 2006). Those high-inclination MBAs remain in the collisional evolution dominated by hypervelocity impacts. The size distribution of high-inclination MBAs enables to examine the Q_D^* law under collisional processes at high velocity.

Terai & Itoh (2011) performed a survey focused on high-inclination small-size MBAs in 9.0-deg^2 fields using the data with a detection limit of $r = 24.0 \text{ mag}$ obtained by 8.2-m Subaru Telescope. They detected 178 MBA candidates with 0.7–7 km in diameter and found that the size distribution of high-inclination MBAs is shallower than that of low-inclination MBAs over a wide diameter range from 0.7 km to 50 km. However, the faint-end slopes in diameter less than 2 km based on the own survey data potentially include large bias due to the non-uniform data taken at sky regions with various ecliptic latitudes and solar phase angles in uneven atmospheric conditions. Actually, the power-law index of the size distribution for low-inclination MBAs is inconsistent with that presented by previous studies (Ivezić et al. 2001; Yoshida & Nakamura 2007).

In this paper, we present the results of an additional survey to determine the size distribution of high-inclination MBAs down to sub-km diameter. We note that the size distribution of MBAs is poorly represented by a single power law. As seen in figure 1, the distribution has significant slope transitions around 3 km, 20 km, and 100 km in diameter, called ‘wavy’ structure (Campo Bagatin et al. 1994; Durda et al. 1998; Davis et al. 2002; O’Brien & Greenberg 2003). For accurate comparison of the power-law slope between the wavy-patterned size distributions, measurements of the distribution shape in the diameter range from sub-km to several km is required to determine the intrinsic slope.

We carried out an uniform wide-field imaging at high ecliptic latitudes using the Subaru Telescope. This survey allows to obtain a large amount of homogeneous data which give three times more sample of small high-inclination MBAs than the previous study. We evaluate the difference of size distribution between low- and high-inclination MBAs considering the wavy structure and taxonomic distribution. The results provide useful clues for understanding the collisional evolution of primordial asteroids in the early solar system, and also that of planetesimals in some debris disks that have been found outside the solar system.

2. ASTEROID SURVEY

2.1. Observations

Our survey was performed on August 24 and 25, 2008 (UT) using the Suprime-Cam mounted on the 8.2-m Subaru Telescope. The Suprime-Cam is a mosaic camera with ten $2k \times 4k$ CCD chips and covers a $34' \times 27'$ field of view with a pixel scale of $0.20''$ (Miyazaki et al. 2002). The data were taken at sky area centered on RA (J2000) = $21^{\text{h}}40^{\text{m}}$ and Dec (J2000) = $+14^{\circ}00'$, within 6° from opposition in ecliptic longitude. The region with ecliptic latitude of around 25° is suitable to detect asteroids with inclination of 15° or higher in the main belt. We imaged 104 fields which contain no bright background objects. Most of the fields overlap the sky coverage of SDSS Data Release 9² (DR9). Each field was visited twice with 240-sec exposures at an interval of 20 min using the r -band filter. The seeing size is ranging $0''.7$ – $1''.0$ in almost all the data. The total surveyed area is 26.5 deg^2 .

2.2. Data Analysis

The images were processed using IRAF produced by the National Optical Astronomy Observatories (NOAO) and SDFRED2 (Ouchi et al. 2004). The standard procedure of data reduction includes overscan subtraction, flat-fielding, correction of geometric distortion, subtraction of sky background, and position matching between two images which were taken at a same field. Moving objects are searched by the image processing technique presented in Terai et al. (2007). The two-visit imaging with a 20-min interval allows to identify MBAs that have sky motion faster than $\sim 30 \text{ arcsec hr}^{-1}$ at near opposition (see figure 2).

We measured the positions and brightness of detected moving objects using the SExtractor (Bertin & Arnouts 1996) and IRAF/APPHOT package, respectively. In the images acquired with 240-sec exposures, most asteroids are trailed as seen in figure 2. For precise photometry, we produced synthetic apertures appropriate to each object through the following procedures. (i) The circular aperture for absolute photometry of point sources in the image is determined. Its radius is set to ~ 2.5 times the full width at half-maximum (FWHM) of point sources. (ii) The motion velocity of the moving object is estimated from the difference between its central coordinates in the two-visit images. (iii) The circular aperture around the object’s center is evenly extended the distance that the object moved during the exposure time in the both directions along the axis of the motion. The ‘moving-circular’ apertures formed in these ways are drawn in figure 2. We estimated the total flux within the given apertures using the POLYPHOT task.

We also conducted photometry on the field stars listed in the SDSS DR9 catalog with $r = 19.0$ – 20.0 mag in the AB system using the same technique for the flux calibration.. The

²<http://www.sdss3.org/dr9/>

magnitude zero-point of each data was determined from the measured total flux and r -band magnitude provided in the catalog. However, the filter transmission of the Suprime-Cam differs from that of SDSS. The difference in r -band magnitude of the field stars, $r_{\text{sup}} - r_{\text{sdss}}$, was corrected with the SDSS color $(r - i)_{\text{sdss}}$ using the transformation equation presented by Fumiaki Nakata,

$$r_{\text{sup}} - r_{\text{sdss}} = -0.00282 - 0.0498(r - i)_{\text{sdss}} - 0.0149(r - i)_{\text{sdss}}^2. \quad (1)$$

The $(r - i)_{\text{sdss}}$ colors of the field stars were derived from the SDSS DR9 catalog. The resulting zero point of the Suprime-Cam filter system was applied to calculate the apparent magnitudes of detected moving objects in the frame.

To obtain the statistically homogeneous sample, we evaluated limiting magnitude of the all data. The detection efficiency was estimated using artificial asteroid trails implanted into the raw data with every 0.2 mag. The fractions of detection were represented by

$$\eta(r) = \frac{A}{2} \left[1 - \tanh \left(\frac{r - m_{50}}{w} \right) \right], \quad (2)$$

where A , m_{50} , and w are the maximum efficiency, half-maximum magnitude, and transition width, respectively (Gladman et al. 1998). Mean A is 0.84 due to the sky coverage of background objects. We defined $r = 24.4$ mag as the limiting magnitude in this survey. We excluded the data with the net detection efficiency $\eta'(r) = \eta(r)/A$ less than 50% at $r = 24.4$ mag. Figure 3 shows the $\eta'(r)$ curves with the minimum (filled circles) and maximum (open circles) values of the selected data at 24.4 mag. The combined $\eta'(r)$ of all the selected data are also plotted (open triangles). The selected data cover 13.6 deg² in actual or 11.4 deg² in effect. Figure 4 shows histograms of the ecliptic longitude from the opposition and ecliptic latitude covered by the selected data.

3. RESULTS

Our exploration found 441 moving objects in the selected data with the 50% detection limit of $r > 24.4$ mag. Figure 5 shows the distribution of their sky motions in the geocentric ecliptic coordinate system. The major group with the negative longitudinal motions of ~ 30 – 45 arcsec hr⁻¹ consists of MBAs, while the clump around 22 arcsec hr⁻¹ corresponds to Jovian Trojans.

At the region with the geocentric ecliptic latitude β and longitude with respect to opposition λ' , the lower inclination limit of detectable asteroids, I_{lim} , is

$$\sin I_{\text{lim}} = \frac{\Delta}{R} \sin \phi, \quad (3)$$

where R is the heliocentric distance, Δ is the geocentric distance, and ϕ is the elongation angle between the Sun and the asteroid given by $\cos \phi = \cos \lambda' \cos \beta$. In the survey area of $\beta \sim 25^\circ$ near the opposition, I_{lim} is around 15° . Asteroids with inclination I_{lim} show no motion along the ecliptic latitude at the opposition field. In contrast, latitudinally-moving asteroids have inclinations higher than I_{lim} . The dotted lines in figure 5 represent the motions of asteroids in circular orbits when they are observed at opposition ($\lambda' = 0^\circ$) and $\beta = 25^\circ$.

3.1. Estimation of Orbital Parameters

Two-visit positioning of moving objects in a night is insufficient for orbit determination. Instead, we estimated semi-major axis and inclination of each asteroid from the sky motion assuming that the orbit is circular, namely, the eccentricity is zero. The adequacy of this assumption is evaluated below. Jedicke (1996) presents the expressions of ecliptic motion derived from orbital elements and sky coordinate (see also the appendix in Ivezić et al. 2001).

Let us consider an asteroid in a circular orbit with semi-major axis a and inclination I located at a heliocentric ecliptic longitude with respect to opposition l' and latitude b . We use the coordinate system defined in figure 2 of Jedicke (1996). The position vector from the Sun, \mathbf{R} , and angular momentum vector, \mathbf{h} , are given by

$$\mathbf{R} = a (\cos l' \cos b, \sin l' \cos b, \sin b), \quad (4)$$

$$\mathbf{h} = \sqrt{\mu a} (\sin \Omega \sin I, -\cos \Omega \sin I, \cos I), \quad (5)$$

respectively, where μ is the product of the gravitational constant and mass of the Sun, and Ω is the longitude of the ascending node derived from l' , b , and I . The relative velocity with respect to the Earth is given by

$$\mathbf{v} = -\frac{\mathbf{R} \times \mathbf{h}}{a^2} - (0, \sqrt{\mu}, 0). \quad (6)$$

The observed ecliptic motion is converted from \mathbf{v} using the unit vectors representing the geocentric directions of increasing ecliptic longitude, latitude, and distance. These vectors are given by

$$\hat{\lambda}' = (-\sin \lambda', \cos \lambda', 0), \quad (7a)$$

$$\hat{\beta} = (-\cos \lambda' \sin \beta, -\sin \lambda' \sin \beta, \cos \beta). \quad (7b)$$

The rates of apparent motion are

$$\dot{\lambda}' = \frac{\mathbf{v}}{\Delta} \cdot \hat{\lambda}', \quad (8a)$$

$$\dot{\beta} = \frac{\mathbf{v}}{\Delta} \cdot \hat{\beta}. \quad (8b)$$

The orbital elements of a detected moving object are derived from the best-fit set of a and I for equation (8b). Several objects with inclinations larger than 40° were excluded because of the significant uncertainty of estimated a and I (see figure 5). Figure 6 shows the distribution of detected asteroids in the semi-major axis vs. inclination space. The dashed curve represents the inclination limit of detectable asteroids given by equation (3). MBAs and Jovian Trojans can be identified clearly. We put objects with $a = 2.0\text{--}3.3$ AU into MBA candidates.

The estimation accuracy of orbital elements of the MBA candidates was evaluated by Monte-Carlo simulation of a virtual asteroid survey. 10,000 hypothetical asteroids were randomly generated in the area of $-5^\circ < \lambda' < +5^\circ$ and $+20^\circ < \beta < +30^\circ$ (see figure 4). The orbit elements

were given in the orbital parameter space ranging $a = 2.3\text{--}3.3$ AU, $e = 0.0\text{--}0.5$, and $I = 15^\circ\text{--}40^\circ$ in inclination. These were governed by the probability distributions based on the orbital distribution of known MBAs with $I > 15^\circ$ listed in the ASTORB database. The simulation showed that the rms errors are 0.14 AU in semi-major axis and 4.5° in inclination, which are comparable to the values presented by Nakamura & Yoshida (2002) for an ecliptic survey. The estimated heliocentric distances have uncertainty of ~ 0.37 AU. We note that the systematic errors in heliocentric distance and inclination are less than 0.05 AU and 0.1° , respectively, which are small enough to be negligible compared to the random errors.

3.2. Estimation of Asteroid Size

The apparent r -band magnitude of the detected moving objects is converted into the absolute magnitude, H_r , by

$$H_r = r - 5 \log(R \cdot \Delta) - P(\alpha), \quad (9)$$

where α is the phase angle, the angle between the Sun and the Earth from the asteroid, and $P(\alpha)$ is the phase function. We used the $P(\alpha)$ expressions presented by Bowell et al. (1989) assuming the slope parameter $G = 0.15$. The phase angles of MBA candidates range from 6° to 14° .

Asteroid diameter D in km is estimated from

$$\log D = 0.2r_\odot - \log \frac{\sqrt{p}}{2(\text{AU}/\text{km})} - 0.2H_r, \quad (10)$$

where r_\odot and p represent the r -band magnitude of the Sun in the AB system and the geometric albedo. In the SDSS photometric system, $r_\odot = -26.91$ mag and $(r - i)_\odot = 0.13$ mag (Fukugita et al. 2011), which are converted into the Suprime-Cam r_\odot by equation (1).

The geometric albedo was assigned the mean value of albedo-known asteroids. MBAs mainly consist of two major groups: redder/brighter asteroids dominated by S-type asteroids and bluer/darker asteroids dominated by C-type asteroids. These are hereinafter called S-like asteroids and C-like asteroids, respectively. We used the mean albedos obtained from the AKARI All-Sky Survey observations, 0.22 for the S-like asteroids and 0.07 for the C-like asteroids (Usui et al. 2011). The mean albedo of total asteroids depends on the number ratio between S- and C-type asteroids which varies with heliocentric distance.

Assuming that the heliocentric distribution of each group is constant with asteroid size, we estimated fractions of the S-/C-type asteroids from the SDSS Moving Object Catalog³ (SDSS MOC; Ivezić et al. 2002). Ivezić et al. (2001) divided asteroids into the two color groups using a color index given by

$$a^* = 0.89(g - r) + 0.45(r - i) - 0.57. \quad (11)$$

³<http://www.astro.washington.edu/users/ivezic/sdssmoc/sdssmoc.html>

We classified the SDSS MOC asteroids with $a^* > 0$ into S-like asteroids, and those with $a^* < 0$ into C-like asteroids. The number ratios of the C-like to S-like derived from the orbit-known asteroids with $I > 15^\circ$ and $D > 5$ km (larger than the limiting size of complete detection for the both types) are 0.5 in the inner belt ranging $R = 2.0$ – 2.5 AU, 1.7 in the middle belt ranging $R = 2.5$ – 3.0 AU, and 10.0 in the outer belt ranging $R = 3.0$ – 3.3 AU. The weighted mean albedos in the inner, middle, and outer belts are 0.17, 0.13, and 0.09, respectively.

As seen in equation (9), H_r is derived from measurements of the apparent r -band magnitude, R , and Δ . The apparent magnitude includes 1σ uncertainties of ~ 0.15 mag at the faint end, namely $r \sim 24$ mag, where σ is the standard deviation. The estimated R and Δ have uncertainties of ~ 0.37 AU (see Section 3.1). These errors cause the uncertainty in H_r of ~ 0.7 mag. It corresponds to a $\sim 30\%$ error in D .

4. DISCUSSION

4.1. Sample Selection

Figure 7 shows the distribution in semi-major axis versus absolute magnitude of the MBA candidates selected in section 3.1. The error bars display the 1σ uncertainty in photometric measurements. The dashed curve represents the limiting magnitude of 50%-complete detection, namely $r = 24.4$ mag. At the outer edge of the main belt defined as $R = 3.3$ AU, the detection limit corresponds to $H_r = 19.4$ mag. We put the MBA candidates with $H_r \leq 19.4$ mag into the final sample including 221 objects for statistical analysis.

Figure 8 shows the number distributions of semi-major axis and inclination for the sample asteroids. Almost all of them have inclinations larger than 14° , allowing to examine the size distribution of high-inclination MBAs. Also, the sample asteroids are mostly located in the outer region of main belt and therefore are likely to be dominated by C-type asteroids (Bus & Binzel 2002).

4.2. Size Distribution

Figure 9 shows the cumulative size distribution (CSD) as a function of asteroid diameter obtained from the final sample. The cumulative number was weighted by the net detection efficiency of each object as $1/\eta'(r)$ (see Section 2.2). The arrow represents the asteroid size converted from the 50% detection limit at $R = 3.3$ AU ($H_r = 19.4$ mag) with the albedo given for the outer-belt asteroids ($p = 0.09$), corresponding to $D = 0.56$ km.

The CSD is represented by a power-law expression as $\Sigma(> D) \propto D^{-b}$, where $\Sigma(> D)$ is the number of asteroids larger than D in diameter per square degree. The power-law index b gives

the CSD slope. We found that the CSD has a knee around $D = 1.0$ km, namely, the slope in $D < 1.0$ km is shallower than that in $D > 1.0$ km. This feature has also been indicated in the previous survey for low-inclination sub-km MBAs by Yoshida & Nakamura (2007). Hence, we fixed two diameter regions, 0.6 km to 1.0 km and 1.0 km to 3.0 km, for characterization of the CSD. The region with $D > 3$ km was excluded because of the large uncertainties.

The CSD slopes were estimated by the maximum likelihood method (e.g. Irwin et al. 1995; Loredó 2004). The differential surface density of asteroids with diameter D km is represented by

$$\Sigma(D) = b \Sigma(> 1 \text{ km}) D^{-b-1}. \quad (12)$$

The likelihood function for n objects is given by

$$L = \exp\left[-\Omega \int \eta(r(D)) \Sigma(D|b) dD\right] \prod_{i=1}^n \sigma(D_i) \Sigma(D_i|b), \quad (13)$$

where Ω is the survey area and $\sigma(D_i)$ is the uncertainty in diameter of object i . The function parameter of the detection efficiency η is derived from that combined with the selected data (see Section 2.2). $r(D)$ denotes the apparent r magnitude converted from D with $R = 2.9$ AU (the mean of the sample) and $p = 0.10$ (weighted mean albedos in the whole main belt with $I > 15^\circ$).

The likelihood analysis gives the slopes of $b = 1.25 \pm 0.03$ (1σ) in $0.6 \text{ km} < D < 1.0 \text{ km}$ and $b = 1.84 \pm 0.27$ in $1.0 \text{ km} < D < 3.0 \text{ km}$. The best-fit power-law CSDs are shown in figure 9. We evaluated the fitting of the power laws using the Anderson-Darling statistic (Anderson & Darling 1952), given by

$$\text{AD} = \int_0^1 \frac{[S(D) - P(D)]^2}{P(D)[1 - P(D)]} dP(D), \quad (14)$$

where $P(D)$ the cumulative detection probability for an object larger than D in diameter, and $S(D)$ is the cumulative distribution function of the detected objects (Bernstein et al. 2004). The goodness of fit is decided by the probability $Pr(\text{AD})$ of a random realization with AD-value higher than the real data. Low $Pr(\text{AD})$ (less than 0.05) implies a poor fit of the distribution. Our calculation found $Pr(\text{AD}) = 0.52$, indicating that the power-law fitting well represents the observed CSD.

Terai & Itoh (2011) presented that $b = 1.79 \pm 0.05$ for MBAs with $I < 15^\circ$ and $b = 1.62 \pm 0.07$ for MBAs with $I > 15^\circ$ in $0.7 \text{ km} < D < 2.0 \text{ km}$. The slope for low- I MBAs is much steeper than that of Yoshida & Nakamura (2007), $b = 1.29 \pm 0.02$ in $0.6 \text{ km} < D < 1 \text{ km}$. This discrepancy seems to be due to significant observational bias caused by the use of mixed data taken in different ecliptic latitudes as well as solar phase angles. In contrast, assuming that b of high- I MBAs is ~ 0.1 smaller than that of low- I MBAs as shown by Terai & Itoh (2011), the result of this study, $b = 1.25$ for high- I MBAs, is consistent with the CSD slope for low- I sub-km MBAs given by Yoshida & Nakamura (2007). It shows a significant improvement in measurement accuracy of the size distribution by an increase of the sample number, appropriate survey fields located around the opposition, homogeneity of the survey region and data quality, and precise photometric calibration using the background SDSS stars.

4.3. Power-law Slope

Finally, we examined the difference in CSD slopes between low- and high- I MBAs. Previous asteroid surveys showed that the size distribution of MBAs exhibits a wavy pattern. This structure is generated by the transition of impact strength between the strength- and gravity-scaled regimes (Davis et al. 1994; O’Brien & Greenberg 2003) as well as possibly by a small-size cutoff due to the Poynting-Robertson drag and solar radiation pressure (Campo Bagatin et al. 1994). In addition, it has been indicated that the CSD slopes are different between S- and C-like asteroids (Ivezić et al. 2001; Yoshida & Nakamura 2007). In order to compare CSD slopes, the size range and number ratio of S- and C-like asteroids should be conformed.

As a representative CSD slope of low- I MBAs, we cited the results of Yoshida & Nakamura (2007). The colorimetric asteroid survey in the field within $\pm 3^\circ$ from the ecliptic plane detected a thousand of small MBAs, most of which have inclinations less than 10° . It presented the CSD slopes of $b = 1.29 \pm 0.02$ in $0.3 \text{ km} < D < 1.0 \text{ km}$ for S-like asteroids and $b = 1.33 \pm 0.02$ in $0.6 \text{ km} < D < 1.0 \text{ km}$ for C-like asteroids. Yoshida & Nakamura (2007) also showed the heliocentric distribution of the both classes. In the outer region beyond $\sim 2.6 \text{ AU}$ where most of the sample asteroids in our survey are distributed, the fraction of S-like asteroids is ~ 0.2 and the other is ~ 0.8 .

We conducted Monte Carlo simulations to estimate the CSD for low-inclination MBAs with given fractions of the two groups. Ten thousands of hypothetical S- and C-like asteroids are generated according to the abundance ratio of 1:4. Each asteroid is given diameter ranging from 0.6 km to 40 km following the differential size distribution $dN/dD \propto D^{-b-1}$ with power-law indexes of -2.29 ± 0.02 for S-like asteroids and -2.33 ± 0.02 for C-like asteroids. The result showed that the compound CSD obeys a power-law distribution with $b = 1.32 \pm 0.02$ in $0.6 \text{ km} < D < 1.0 \text{ km}$. It is significantly steeper than that obtained from our survey, $b = 1.25 \pm 0.03$, with the difference of $\Delta b = 0.07 \pm 0.04$. We confirmed that the high-inclination MBAs have a shallow CSD compared to the low-inclination MBAs at least in sub-km size range.

On the other hand, it is difficult to compare the CSDs between Yoshida & Nakamura (2007) and this study in the larger size range of $D > 1.0 \text{ km}$ because of large uncertainty due to small number of the samples and loss of some unmeasurable objects which are bright enough to reach saturation. Instead, we analyzed the SDSS MOC including astrometric and photometric data for 471,569 moving objects. As in the case of our survey, most of them are unknown asteroids in orbit and albedo. We estimate orbital elements and absolute magnitude of each SDSS MOC object using the same methods and assumptions as this study (see section 3.1 and 3.2).

The SDSS MOC objects are classified according to the following definitions: (i) MBAs are objects with $a = 2.1\text{--}3.3 \text{ AU}$. (ii) S-like asteroids are objects with $a^* > 0$, and C-like asteroids are objects with $a^* < 0$, where a^* is the color index defined by equation (11). (iii) Low-inclination asteroids are objects with $I < 15^\circ$, and high-inclination asteroids are objects with $I > 15^\circ$. Diameter of each MBA is estimated assuming $p = 0.22$ for objects with $a^* > 0$ as S-like asteroids and $p = 0.07$ for objects with $a^* < 0$ as C-like asteroids. The SDSS MOC seems to keep the complete detection

up to $r = 21.2$ mag corresponding to $D \leq 2.0$ km (Parker et al. 2008). In $2.0 \text{ km} < D < 5.0$ km, the CSDs of SDSS MOC MBAs have $b = 2.65 \pm 0.03$ for the low-inclination S-like, $b = 2.17 \pm 0.04$ for the high-inclination S-like, $b = 2.24 \pm 0.02$ for the low-inclination C-like, and $b = 2.01 \pm 0.02$ for the high-inclination C-like. We confirmed that high-inclination MBAs have a shallower CSD in either class.

Then, model CSDs were generated from a mixture of the S-like and C-like MBAs with a number ratio of 1:4 in each inclination population. The estimation of CSD slopes in $2.0 \text{ km} < D < 5.0$ km gives $b = 2.31 \pm 0.02$ for the low-inclination MBAs and $b = 2.04 \pm 0.02$ for the high-inclination MBAs. The difference of the slopes, $\Delta b = b(I < 15^\circ) - b(I > 15^\circ)$, is 0.27 ± 0.03 , much larger than the value indicated in our survey ($\Delta b = 0.07 \pm 0.04$). The discrepancy in Δb between the two size ranges can be explained by the difference of wavy pattern in CSDs. We discuss the interpretations of this result in the following section.

4.4. Impact Strength Law

O’Brien & Greenberg (2003) presented an analytical model for steady-state size distributions resulting from a collisional cascade with the following two essential facts. First, the primary component of CSD slope represented by a single power-law index b_p is given by a simple expression of

$$b_p = \frac{5}{2 + s/3}, \quad (15)$$

where s is the power-law index of the Q_D^* law, namely $Q_D^* \propto D^s$. Second, the transition of the Q_D^* law at a diameter of $D_t = 0.1\text{--}1.0$ km induces the wavy structure on the MBA size distribution. In the gravity-scaled regime ($D > D_t$), the index s_g is positive, i.e. $b_p < 2.5$. Conversely, in the strength-scaled regime ($D < D_t$), the index s_s is negative, i.e. $b_p > 2.5$. The inflection in the Q_D^* law results wavelike oscillations about the CSD power law with an index b_p in the gravity-scaled regime. The CSD shape in $D > D_t$ is determined by the primary slope b_p as well as the phase and amplitude of the wave pattern. O’Brien & Greenberg (2005) found that the Q_D^* law with $s_g \approx 1.40$ and $D_t \approx 0.2$ km reproduces the observed MBA size distribution.

The diameter range of CSD measurements in this study is 0.7–5.0 km covering from the first bump down from D_t . Terai & Itoh (2011) confirmed no significant difference in the peak/valley positions of the CSDs’ wavy pattern between low- and high-inclination MBAs. We suggest a simple model that the CSD shape varies only with b_p and the wave amplitude between the two populations. The difference between a CSD slope in a local size range and the primary slope, $|b - b_p|$, is assumed to shift in proportion to wave amplitude. When the wave amplitude increases k times, b becomes $k(b - b_p) + b_p$. This model allows to briefly express the relationships between b_p and the estimated CSD slopes, $b_{1,L}$, $b_{2,L}$, $b_{1,H}$, $b_{2,H}$, where the suffix 1 and 2 show the diameter ranges of 0.6–1.0 km and 2.0–5.0 km, respectively, and the suffix L and H show the low- and high-inclination populations, respectively

The MBAs’ Q_D^* law with $s_g = 1.40$ (O’Brien & Greenberg 2005) derives $b_p = 2.03$ using equation (15). It corresponds to the primary CSD slope of low-inclination MBAs. The relational expressions of the CSD indexes in this model are given by

$$b_{i,H} - b_{p,H} = k(b_{i,L} - b_{p,L}), \quad i = 1, 2, \quad (16)$$

where $b_{p,L}$ and $b_{p,H}$ are the primary CSD slopes for low- and high-inclination MBAs, respectively ($b_{p,L} = 2.03$). Our analysis showed the local CSD slopes of $b_{1,L} = 1.32 \pm 0.02$, $b_{2,L} = 2.31 \pm 0.02$, $b_{1,H} = 1.25 \pm 0.03$, and $b_{2,H} = 2.04 \pm 0.02$. Those give the solution of equation (16) that $b_{p,H} = 1.82 \pm 0.07$ and $k = 0.80 \pm 0.04$. This $b_{p,H}$ value is converted into $s_g = 2.2 \pm 0.3$ when equation (15) is applied. However, the collisional evolution of high-inclination MBAs is dominated by collisions with low-inclination asteroids though equation (16) is based on collisional equilibrium in a self-contained system (O’Brien & Greenberg 2003). Numerical simulations for the collisional evolution are required to derive s_g from $b_{p,H}$. But anyway, the result in $b_{p,H} < b_{p,L}$ indicates a steep Q_D^* law in the gravity-scaled regime of high-inclination MBAs. It leads to the conclusion that hypervelocity collisions on large bodies are relatively less disruptive. This may suggest that the inelasticity parameter determining the fraction of impact energy partitioned into fragment kinetic energy, generally denoted by f_{KE} (Campo Bagatin et al. 2001; O’Brien & Greenberg 2005), decreases with collision velocity around several km sec^{-1} .

Our results imply that the collisional evolution and the resulting size distribution of an asteroid population suffered hypervelocity collisions are not the same as those of ecliptic MBAs even if the compositions and internal structures are similar to each other. In the inner region of planetesimal disk after formation of giant planets and gas dissipation, small bodies are dynamically excited and collide with each another at high velocities. Bottke et al. (2005b) showed that in the primordial main belt zone during the dynamical excitation phase caused by planetary embryos and Jupiter, collisions between remnant asteroids occur at $6\text{--}8 \text{ km sec}^{-1}$ and collisions between remnant asteroids and depleted asteroids reach more than 10 km sec^{-1} . The velocity-dependent Q_D^* law should be introduced for investigating the ancient size distribution and its evolution of asteroids at the final stage of planet formation processes. It allows to more precisely estimate the impact rate and size distribution of meteorites colliding with the Earth and moon in the early solar system.

Besides high-inclination MBAs, near-Earth asteroids (NEAs) collide with each other at greater than 10 km sec^{-1} (Bottke et al. 1994). Jovian Trojans with high inclinations ($I \gtrsim 20^\circ$) also have mean collision velocities of $\sim 6 \text{ km sec}^{-1}$ or higher (Marzari et al. 1996). In addition, high-velocity collisional processes were confirmed in several planetesimal disks such as HD172555 (Lisse et al. 2009) and Epsilon Eridani systems (Th ebault et al. 2002).

The relationship between Q_D^* law and collision velocity is required to be determined by combination of further studies with observations, numerical simulations, and laboratory experiments. It provides insight into the collisional evolution of small-body populations located in the regions close to the host star or distant from the ecliptic plane, as well as in the systems around a massive star or containing giant planets.

5. CONCLUSIONS

Our survey detected 441 asteroids in 13.6 deg^2 at high ecliptic latitudes with a 50% limiting magnitude of $r = 24.4 \text{ mag}$. We obtained an unbiased sample consisting of 221 MBA candidates with inclination of $I \gtrsim 14^\circ$ and absolute magnitude of $H_r \leq 19.4 \text{ mag}$. Although orbits and diameters of each asteroid cannot be determined and instead are estimated with the assumption of a circular orbit and given albedo depending on radial regions, the sample yields a sufficiently quality CSD to measure its slope in sub-km size.

The CSD for high-inclination MBAs shows a roll-over at $D \sim 1.0 \text{ km}$ which has also been indicated by Yoshida & Nakamura (2007) for low-inclination MBAs. The maximum likelihood analysis provided the best-fit power laws with $b = 1.25 \pm 0.03$ in $0.6 \text{ km} < D < 1.0 \text{ km}$ and $b = 1.84 \pm 0.27$ in $1.0 \text{ km} < D < 3.0 \text{ km}$. Most of the MBA candidates are located beyond 2.6 AU where Yoshida & Nakamura (2007) showed the abundance ratio of S- and C-like asteroids is 1:4 for low-inclination sub-km MBAs. The compound CSD with the number ratio of 1:4 has $b=1.32 \pm 0.02$ in $0.6 \text{ km} < D < 1.0 \text{ km}$, indicating that high-inclination MBAs have a shallower CSD in sub-km size.

We furthermore examined the CSDs in $2.0 \text{ km} < D < 5.0 \text{ km}$ using the SDSS MOC database. The slopes are $b = 2.31 \pm 0.02$ for low-inclination MBAs and $b = 2.04 \pm 0.02$ for high-inclination asteroids. Although high-inclination MBAs have shallower CSDs in both of the size ranges, the slope difference is larger in the larger size. This inconsistency is explained to be due to the difference of the wavy pattern on CSDs between low- and high-inclination populations. Assuming a simple model that the both populations have the same positions of ‘bump’ on the CSDs at a few-km diameter, high-inclination MBAs have a primary CSD slope of $b_p=1.82 \pm 0.07$ over the diameter range from 0.6 km to 5.0 km. It is definitely shallower than that of low-inclination MBAs, indicating that hypervelocity collisions raises the relative strength of large bodies against catastrophic impacts.

We thank Melissa McGrath for providing valuable comments. This study is based on data collected at Subaru Telescope. T. Terai was supported by the Grant-in-Aid from Japan Society for the Promotion of Science (20-4879).

Facilities: Subaru Telescope (NAOJ).

REFERENCES

- Anderson T. W., & Darling, D. A. 1952, *Annals of Mathematical Statistics*, 23, 193
- Benz, W., & Asphaug, E. 1999, *Icarus*, 142, 5
- Bernstein, G. M., Trilling, D. E., Allen, R. L., et al. 2004, *AJ*, 128, 1364
- Bertin, E., & Arnouts, S. 1996, *A&AS*, 117, 393

- Bottke, W. F., Jr., Nolan, M. C., Greenberg, R., & Kolvoord, R. A. 1994, Hazards Due to Comets and Asteroids, 337
- Bottke, W. F., Durda, D. D., Nesvorný, D., et al. 2005, *Icarus*, 175, 111
- Bottke, W. F., Durda, D. D., Nesvorný, D., et al. 2005, *Icarus*, 179, 63
- Bowell, E., Hapke, B., Domingue, D., et al. 1989, *Asteroids II*, 524
- Bowell, E., Muinonen, K., & Wasserman, L. H. 1994, *Asteroids, Comets, Meteors 1993*, 160, 477
- Bus, S. J., & Binzel, R. P. 2002, *Icarus*, 158, 146
- Campo Bagatin, A., Cellino, A., Davis, D. R., Farinella, P., & Paolicchi, P. 1994, *Planet. Space Sci.*, 42, 1079
- Campo Bagatin, A., Petit, J.-M., & Farinella, P. 2001, *Icarus*, 149, 198
- Davis, D. R., Ryan, E. V., & Farinella, P. 1994, *Planet. Space Sci.*, 42, 599
- Davis, D. R., Durda, D. D., Marzari, F., Campo Bagatin, A., & Gil-Hutton, R. 2002, *Asteroids III*, 545
- de Elía, G. C., & Brunini, A. 2007, *A&A*, 466, 1159
- Durda, D. D., Greenberg, R., & Jedicke, R. 1998, *Icarus*, 135, 431
- Farinella, P., & Davis, D. R. 1992, *Icarus*, 97, 111
- Fukugita, M., Ichikawa, T., Gunn, J. E., Doi, M., Shimasaku, K., & Schneider, D. P. 1996, *AJ*, 111, 1748
- Fukugita, M., Yasuda, N., Doi, M., Gunn, J. E., & York, D. G. 2011, *AJ*, 141, 47
- Gil-Hutton, R. 2006, *Icarus*, 183, 93
- Gladman, B., Kavelaars, J. J., Nicholson, P. D., Loredó, T. J., & Burns, J. A. 1998, *AJ*, 116, 2042
- Gladman, B. J., Davis, D. R., Neese, C., et al. 2009, *Icarus*, 202, 104
- Housen, K. R., & Holsapple, K. A. 1990, *Icarus*, 84, 226
- Ivezić, Ž., Tabachnik, S., Rafikov, R., et al. 2001, *AJ*, 122, 2749
- Ivezić, Ž., Jurić, M., Lupton, R. H., Tabachnik, S., & Quinn, T. 2002, *Proc. SPIE*, 4836, 98
- Irwin, M., Tremaine, S., & Zytzkow, A. N. 1995, *AJ*, 110, 3082
- Jedicke, R. 1996, *AJ*, 111, 970

- Jedicke, R., & Metcalfe, T. S. 1998, *Icarus*, 131, 245
- Jutzi, M., Michel, P., Benz, W., & Richardson, D. C. 2010, *Icarus*, 207, 54
- Kadono, T., Sakaiya, T., Hironaka, Y., et al. 2010, *Journal of Geophysical Research (Planets)*, 115, 4003
- Lisse, C. M., Chen, C. H., Wyatt, M. C., et al. 2009, *ApJ*, 701, 2019
- Loredo, T. J. 2004, *American Institute of Physics Conference Series*, 735, 195
- Marzari, F., Scholl, H., & Farinella, P. 1996, *Icarus*, 119, 192
- Masiero, J. R., Mainzer, A. K., Grav, T., et al. 2011, *ApJ*, 741, 68
- Miyazaki, S., Komiyama, Y., Sekiguchi, M., et al. 2002, *PASJ*, 54, 833
- Nakamura, T., & Yoshida, F. 2002, *PASJ*, 54, 1079
- O’Brien, D. P., & Greenberg, R. 2003, *Icarus*, 164, 334
- O’Brien, D. P., & Greenberg, R. 2005, *Icarus*, 178, 179
- Ouchi, M., Shimasaku, K., Okamura, S., et al. 2004, *ApJ*, 611, 660
- Parker, A., Ivezić, Ž., Jurić, M., et al. 2008, *Icarus*, 198, 138
- Petit, J.-M., Morbidelli, A., & Chambers, J. 2001, *Icarus*, 153, 338
- Takasawa, S., Nakamura, A. M., Kadono, T., et al. 2011, *ApJ*, 733, L39
- Tedesco, E. F., Noah, P. V., Noah, M., & Price, S. D. 2002, *AJ*, 123, 1056
- Terai, T., Itoh, Y., & Mukai, T. 2007, *PASJ*, 59, 1175
- Terai, T., & Itoh, Y. 2011, *PASJ*, 63, 335
- Thébault, P., Marzari, F., & Scholl, H. 2002, *A&A*, 384, 594
- Usui, F., Kuroda, D., Müller, T. G., et al. 2011, *PASJ*, 63, 1117
- van Houten, C. J., van Houten-Groeneveld, I., Herget, P., & Gehrels, T. 1970, *A&AS*, 2, 339
- Vedder, J. D. 1998, *Icarus*, 131, 283
- Yoshida, F., Nakamura, T., Watanabe, J.-I., et al. 2003, *PASJ*, 55, 701
- Yoshida, F., & Nakamura, T. 2007, *Planet. Space Sci.*, 55, 1113

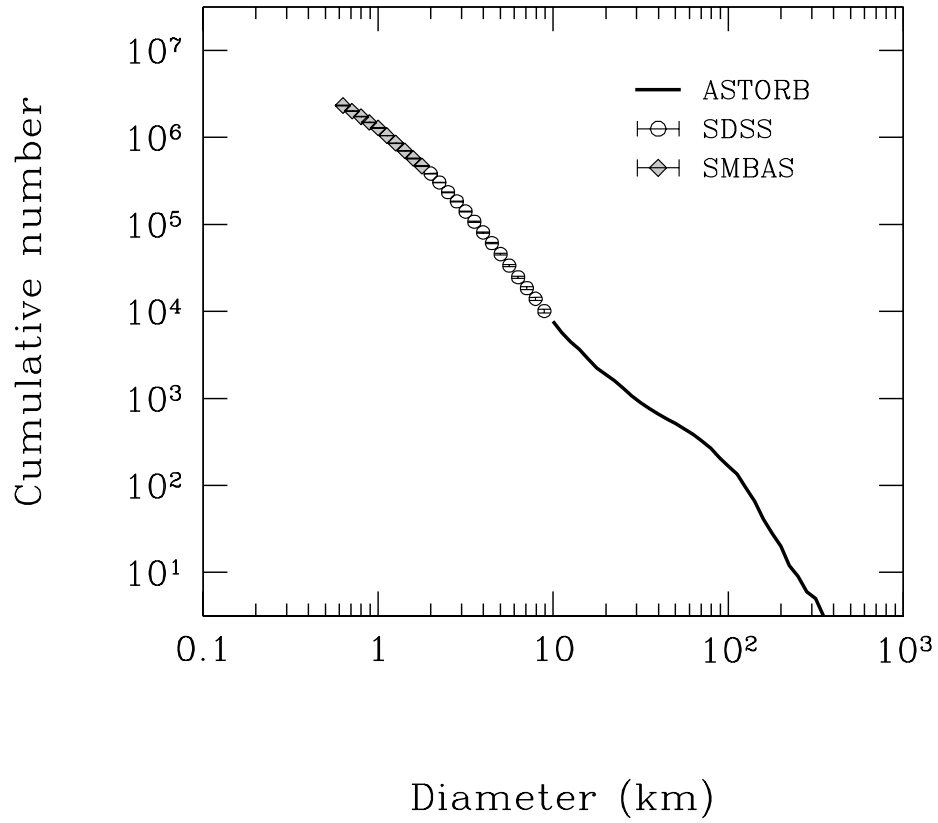


Fig. 1.— The cumulative size distribution of main-belt asteroids estimated from the previous observations. The solid line represents the population of observed asteroids listed in the ASTORB database (Bowell et al. 1994). The circles and diamonds represent extrapolations based on the results of the Sloan Digital Sky Survey (Ivezić et al. 2001) and Subaru Main Belt Asteroid Survey (Yoshida & Nakamura 2007), respectively.

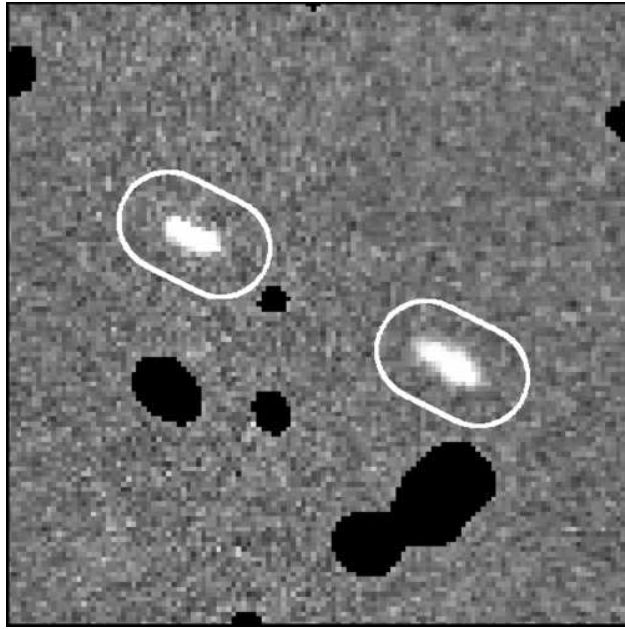


Fig. 2.— Detected moving objects in the combined image from two-visit images. The original images were taken with 240-sec exposures at an interval of 20 min under a seeing size of 0.8 arcsec. The field of view covers $25'' \times 25''$ with north up and east to the left. The background objects have been masked (black regions). The moving objects have a sky motion of $38 \text{ arcsec hr}^{-1}$ and brightness of $r = 23.07 \pm 0.07 \text{ mag}$. The circles surrounding the objects show the apertures for photometry.

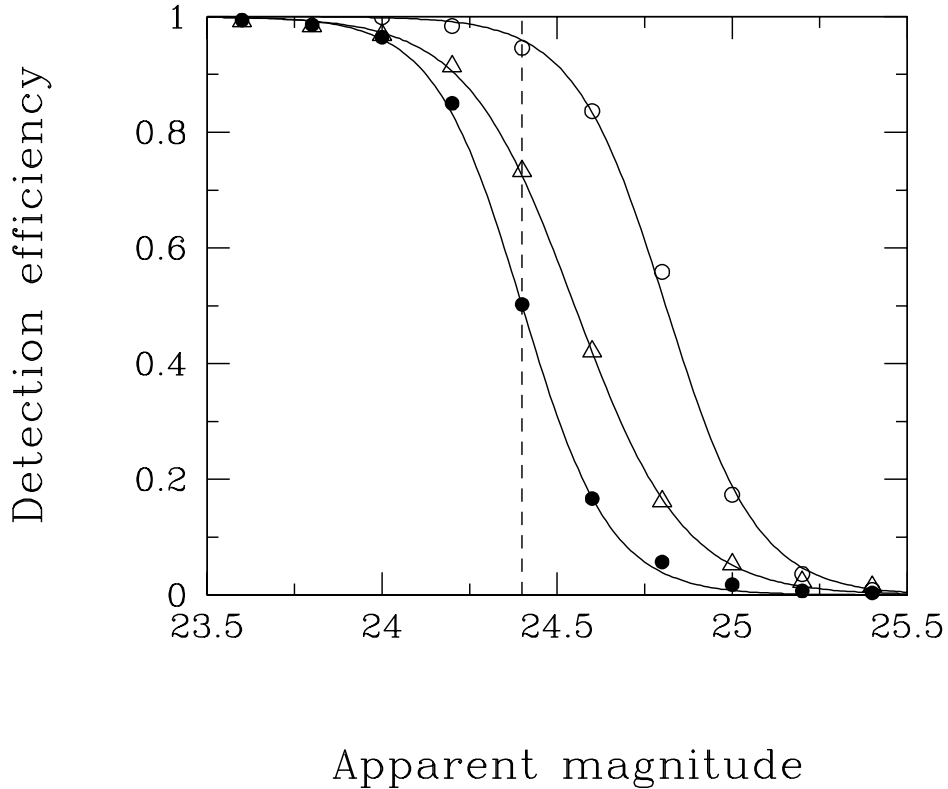


Fig. 3.— Net detection efficiency $\eta'(r)$ for moving objects as a function of apparent r magnitude. The detection efficiency reduces with motion velocity due to the decrease in flux density. In this work, the motion velocity was set to $40 \text{ arcsec hr}^{-1}$, similar to or faster than those of most of the detected MBA candidates (see figure 5 and 6). Only the data with $\eta'(r) \geq 0.5$ at $r = 24.4 \text{ mag}$ was used for our analysis of the asteroid population. The filled circles and open circles represent objects with the minimum and maximum $\eta'(r)$ at $r = 24.4 \text{ mag}$ (dashed line) in the selected data, respectively. The open triangles show combined $\eta'(r)$ of all the selected data. This curve indicates that objects even with close to $r = 24.4 \text{ mag}$ can be detected with efficiencies of about 0.7 or higher in most of the images. The faintest objects in our sample cause little increase in statistical uncertainty of measurement of the size distributions. The solid curves are best-fit functions given by equation (2).

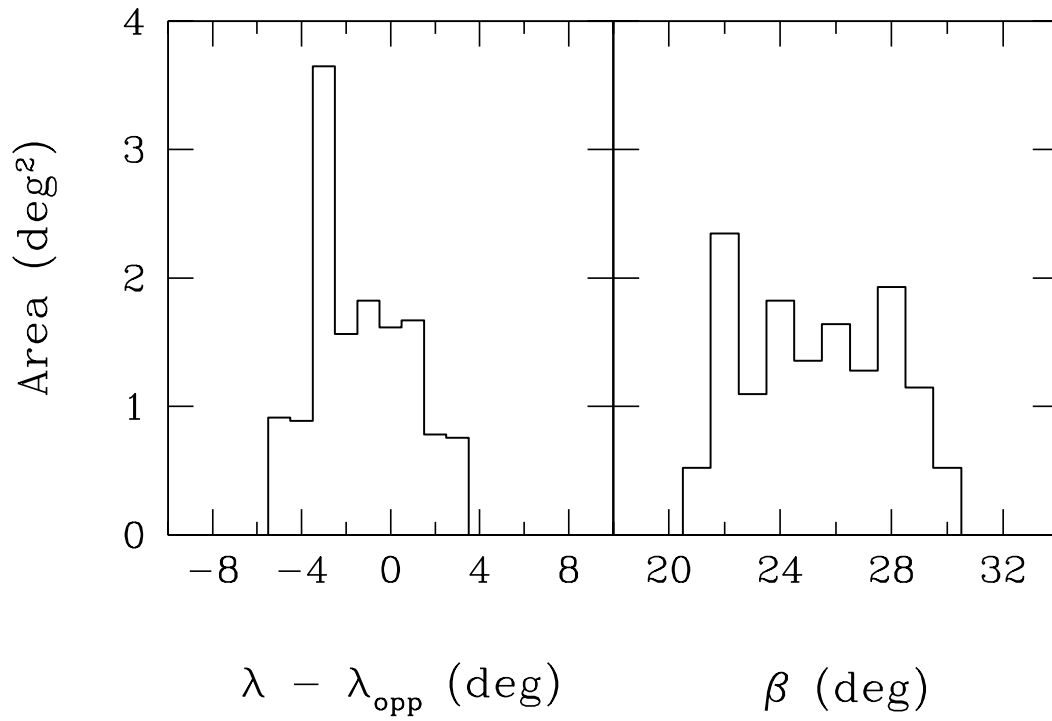


Fig. 4.— Distributions of the ecliptic longitude with respect to opposition ($\lambda - \lambda_{\text{opp}}$; left) and ecliptic latitude (β ; right) covered by the selected data.

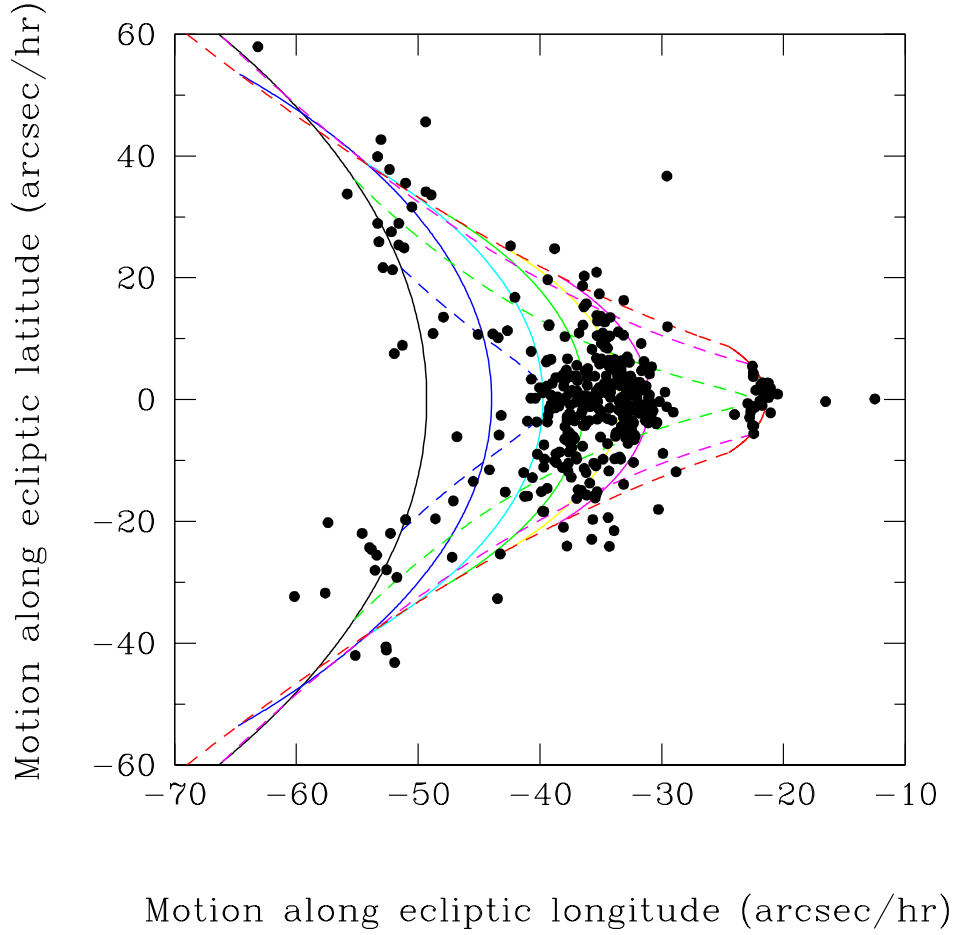


Fig. 5.— Sky motion distribution in the ecliptic coordinate system for moving objects detected in this survey. The solid lines represent motions of asteroids in circular orbits with semi-major axes of 1.8 AU (black), 2.1 AU (blue), 2.4 AU (cyan), 2.7 AU (green), 3.0 AU (yellow), 3.3 AU (magenta), and 5.2 AU (red) at the ecliptic longitude of opposition and latitude of $+25^\circ$. The dashed lines represent motions of asteroids in circular orbits with inclinations of 15° (blue), 20° (green), 30° (magenta), and 40° (red) at the ecliptic longitude of opposition and latitude of $+25^\circ$.

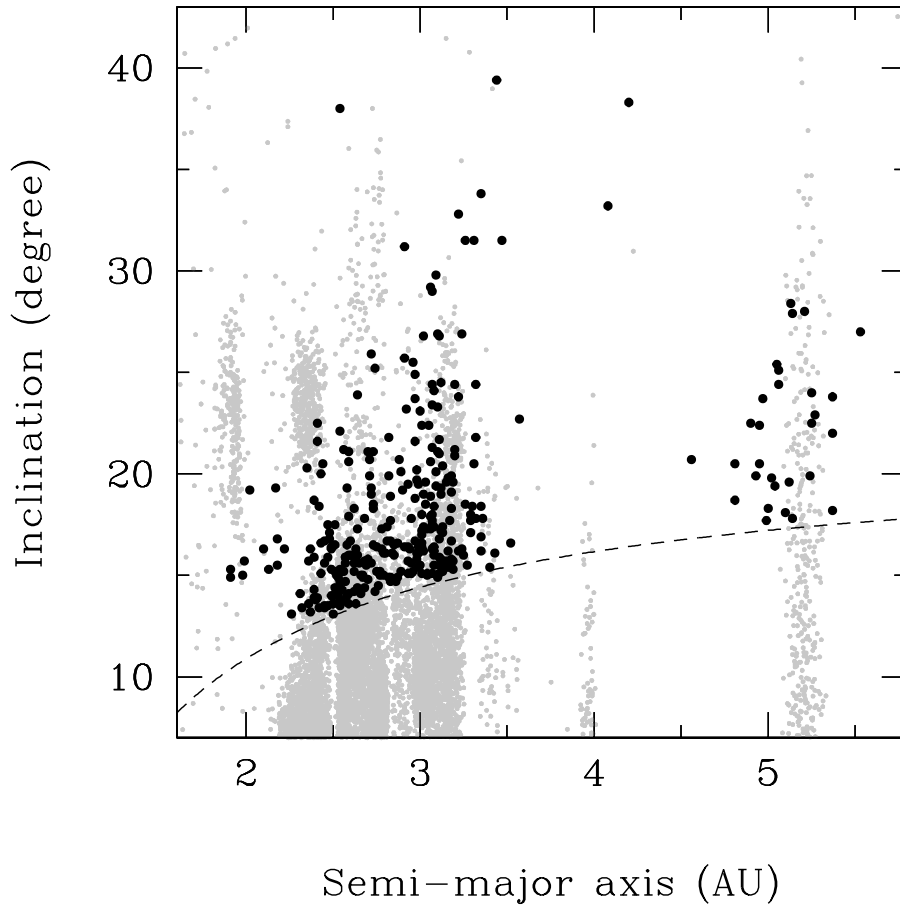


Fig. 6.— Estimated semi-major axes and inclinations of moving objects detected in this survey assuming circular orbits (black dots). The major swarm consists of main-belt asteroids. The minor swarm around 5 AU corresponds to the Jovian Trojan group. The orbits of 50,000 known asteroids are also plotted as gray dots. The dashed curve shows the detection limit given by the lowest ecliptic latitude ($+21^\circ$) in the survey fields.

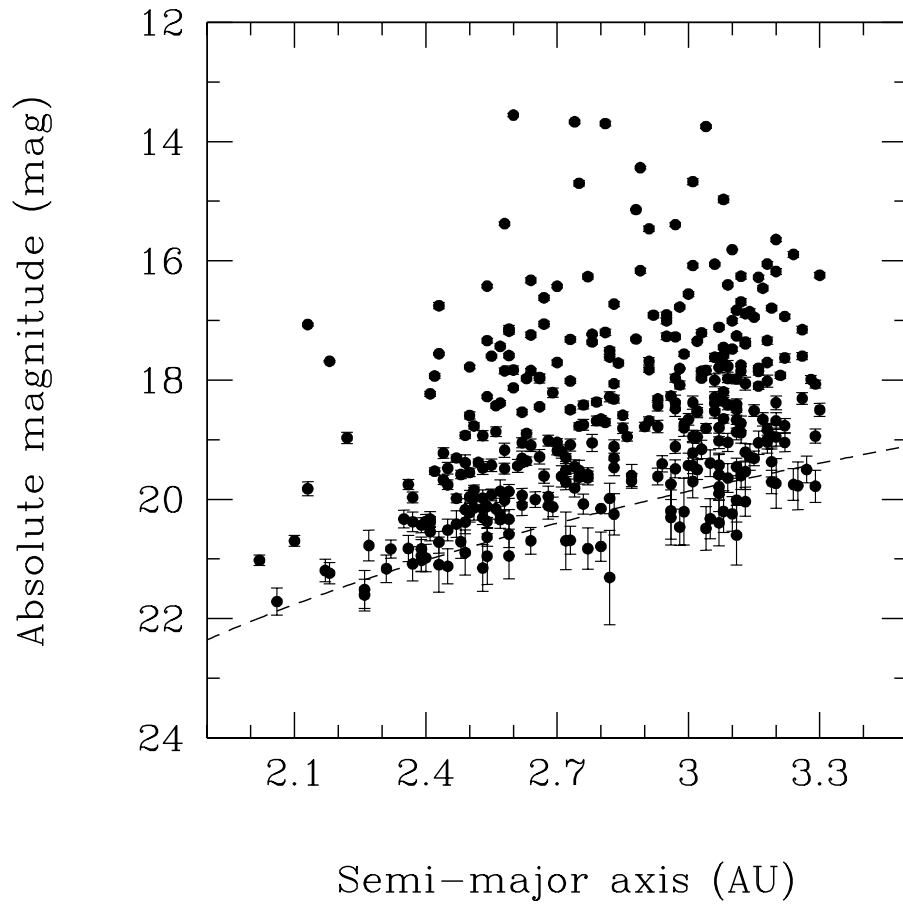


Fig. 7.— Plot of estimated semi-major axis vs. absolute r magnitude in the AB system for the main-belt asteroid candidates. The error bars represent photometric uncertainty. The dashed curve shows the 50%-complete detection limit corresponding to apparent magnitude of $r = 24.4$ mag.

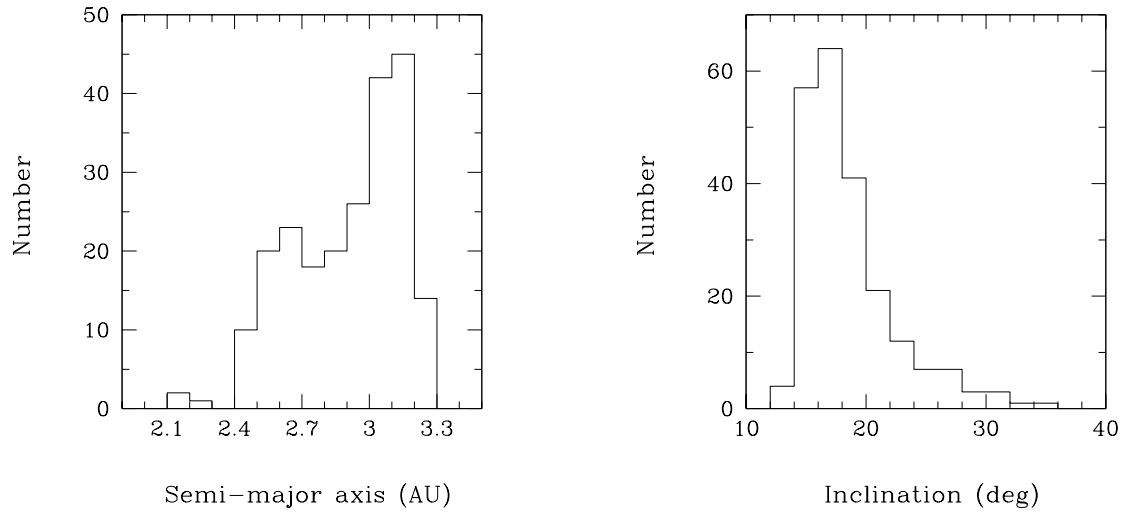


Fig. 8.— Number distributions of estimated semi-major axis (left) and inclination (right) for the final sample of MBA candidates with $H_r \leq 19.4$ mag (H_r is absolute r magnitude in the AB system).

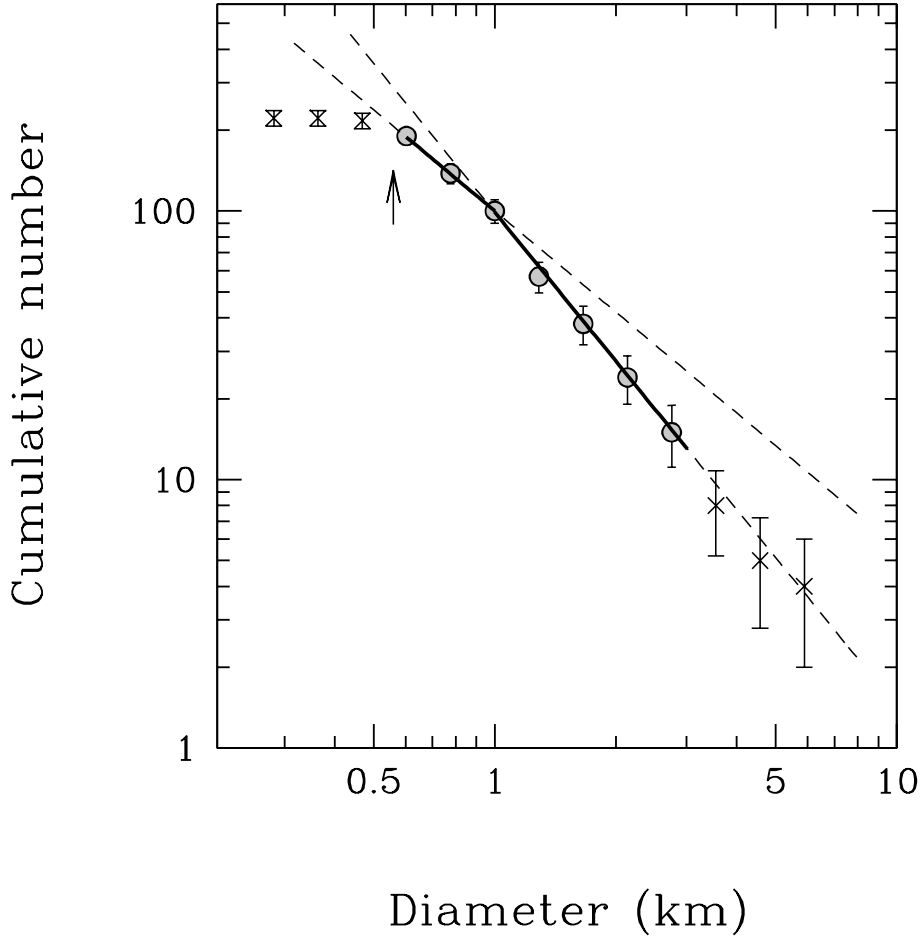


Fig. 9.— Cumulative size distribution of the MBA sample. The cumulative number $N(>D)$, where D is diameter in km, has been corrected for detection efficiency. The error bars represent \sqrt{N} , where N is the cumulative number. The data points in the fitting regions are plotted as circles, while those excluded from the fitting are plotted as cross signs. The straight lines show the best-fit power-law functions in $0.6 \text{ km} < D < 1.0 \text{ km}$ and $1.0 \text{ km} < D < 3.0 \text{ km}$. The arrow shows the detection limit, $D = 0.56 \text{ km}$ (see text).